




Reactive transverse waves in a near-limit detonation

Mark D. Frederick¹ , Rohan M. Gejji¹ , Joseph E. Shepherd²  and Carson D. Slabaugh¹ 

¹School of Aeronautics and Astronautics, Purdue University, West Lafayette, IN 47907, USA

²Graduate Aerospace Laboratories, California Institute of Technology, Pasadena, CA 91125, USA

Corresponding author: Mark D. Frederick, mfrederick@purdue.edu

(Received 6 July 2024; revised 9 June 2025; accepted 21 June 2025)

The reactivity of transverse waves in detonations of methane, oxygen and nitrogen are experimentally assessed using MHz rate schlieren and chemiluminescence imaging. In these highly unstable mixtures, the mode of wave propagation is more complex than what is described by the cellular instability model that is conventionally used for weakly unstable mixtures. Behind the low-speed leading shock in unstable waves, the processed gas remains essentially unreacted until transverse waves reach this region. In highly unstable waves, the transverse waves have a range of reactivity, that is rates of reaction in the flow immediately behind the wave. In this study, we present examples of transverse waves for near-limit detonations and analyse four cases in detail. In some cases, these waves appear to be essentially non-reactive or cause very slow reaction. In other cases, the transverse waves can be highly reactive. In the most extreme example, the transverse wave is propagating at the Chapman–Jouguet speed with a small reaction zone, i.e. a transverse detonation. A reactive oblique shock model is used to approximate the triple-point configuration of this case as a double-Mach reflection, which shows good agreement with the images. The reaction evolution along path lines is analysed using detailed reaction mechanisms and considerations about flow-field unsteadiness. Length scales of the energy release and expansion processes within the reaction zone region are used to explain the observed modes of wave propagation and interaction.

Key words: detonations, high-speed flow, nonlinear instability

1. Introduction

Spatial and temporal oscillations along the leading front of a detonation characterise the coupling between the gas-dynamic and chemical-kinetic aspects of the flow. In the classical cellular instability depiction of an unsupported detonation, the leading shock wave is attached to a reaction zone along high-speed portions of the front and the energy released in the reaction zone sustains the shock. The high-speed portions of the shock decay and eventually decouple from the reaction front due to unsteady effects (Eckett, Quirk & Shepherd 2000) and transition into low-speed portions. Along these low-speed portions, gases that are processed by the leading shock may remain unreacted for some distance behind the front. Transverse waves originating at the junction of the high- and low-speed shocks move laterally along the leading shocks. In multi-front waves, collision of transverse waves of opposite families may create an explosion immediately behind the front that accelerates the leading wave, generating a new high-speed shock and transverse waves, resulting in quasi-periodic oscillation of the leading shock and the characteristic regular cellular pattern. This model is appropriate for describing mixtures that are characterised by relatively weak coupling between the chemical energy release and flow. However, as the coupling between energy release and flow becomes more sensitive to variations in post shock temperature, the detonation front becomes more unstable, resulting in increasingly irregular cellular patterns (Austin & Shepherd 2003; Shepherd 2009; Frederick *et al.* 2023).

The extent of detonation front instability and pattern regularity are useful concepts that are prevalent in the literature but challenging to quantify. In addition to producing oscillations in the leading shock front and axial dynamics, the unstable coupling between the flow and chemical reactions results in strong transverse motion and shock waves. The transverse flow and waves are usually constrained by the boundaries of the confining channel or tube, particularly for mixtures with sufficiently large reaction zones in comparison with the channel or tube transverse dimensions. As a consequence, the extent and regularity of the resulting instability depends both on the mixture and the confining geometry. Nevertheless, clear differences in the instability regimes can be observed from soot foil patterns, schlieren and planar laser-induced fluorescence images, and the power spectra of the leading front oscillations. The extent of instability can be correlated with thermodynamic parameters such as heat capacity and energy release and idealised reaction zone parameters such as non-dimensional activation energy (Austin & Shepherd 2003) and one-dimensional reaction lengths (Ng *et al.* 2005). We have chosen to study a mixture containing methane, oxygen and nitrogen that has been previously characterised (Frederick *et al.* 2022) as highly unstable, both visually and by the parameters listed above.

In our study, we have used a narrow channel geometry and a mixture with a sufficiently large reaction zone to constrain the transverse motion so that the large-scale features are two-dimensional. As a consequence, we are able to observe in detail isolated transverse waves and flow processes behind the leading shock front. The conditions we are studying are often referred to as ‘near-limit’ or ‘marginal’ detonations. The leading shock front has large amplitude oscillations that result in extended unreacted regions behind the low-speed portions of the leading front. These shocked-unreacted regions may be traversed by strong transverse shock waves. This situation is similar to that observed in cylindrical channels with near-limit mixtures in which the limiting case is of a single transverse wave that rotates around the axis of symmetry, creating a ‘spinning’ detonation (Voytsekhovskiy, Mitrofanov & Topchiyan 1963; Schott 1965). An extended shocked, but unreacted, region is created, which is consumed by a rotating, transversely propagating shock wave in the form of a detonation moving through the shocked but unreacted gas. There is substantial

literature on these cases and the related situation of near-limit waves in rectangular channels. A review of recent progress in numerical simulation is found in Takeshima *et al.* (2020), Zhang *et al.* (2024) and Kohama *et al.* (2024).

The goal of the present study is to examine the combustion mechanisms of the gas processed by the low-speed shock. In order for the average speed of the wave to remain at or near the Chapman-Jouguet speed (U_{CJ}), which has been shown to be the case in unstable mixtures (Frederick *et al.* 2023), a substantial fraction of the gases that pass behind the low-speed shock must react before receding too far behind the front. For example, Kiyanda & Higgins (2013) experimentally estimated that in a stoichiometric methane-oxygen planar detonation, only 40 %–50 % of reactants are processed by the high-speed shock and react while directly attached to the front. The remainder pass through the low-speed shock and are too cool to promptly react. One current theory is that these gases accumulate into regions or ‘pockets’ that form along the shear layer between the high-speed shock and transverse wave. Upon collision of the transverse waves, these pockets detach from the front and exist as ‘unburned pockets’ behind the front. One possible combustion mechanism of these remaining reactants is turbulent combustion (Arienti & Shepherd 2005; Radulescu *et al.* 2007) due to mixing of adjacent regions of burned and unburned regions. In order for the energy release from combustion of the reactants in these pockets to contribute to the volumetric expansion that propels the detonation wave, combustion must occur before the pockets are too far behind the front. The critical distance is usually identified as the effective ‘sonic surface’ or ‘hydrodynamic thickness’, which has been estimated to be about 4–7 cell sizes (λ) downstream of the front (Edwards, Jones & Phillips 1976; Radulescu *et al.* 2007). It has been observed in some experiments and simulations that unburned pockets do exist and dissipate within this 4–7 λ region (Radulescu *et al.* 2007).

The transverse waves play an important role in consuming the reactants that persist behind the low-speed shock. Turbulence generated from the collision of these waves induces the necessary mixing for initiating combustion of the unreacted pockets (Radulescu & Lee 2002; Lau-Chapdelaine, Xiao & Radulescu 2020; Sow, Lau-Chapdelaine & Radulescu 2021). The transverse waves themselves may also initiate reaction, such as in the case of some weakly unstable mixtures (Subbotin 1975*a*). In the special case where the detonation is at the limits of propagation, the transverse wave may itself become a detonation, propagating in a self-sustained fashion through the shocked but unburned gas behind the low-speed shock. This was first observed by Strehlow & Crooker (1974) in a rectangular channel with a mixture of hydrogen/oxygen/argon at low pressure. Transverse propagation of detonations are observed experimentally in many cases where the detonation is near the limit of self-sustained propagation, such as through divergent channels (Gamezo *et al.* 2000), diffraction (Pintgen & Shepherd 2009; Bhattacharjee *et al.* 2013), porous media (Radulescu & Maxwell 2011) and lateral strain (Xiao & Radulescu 2020*a,b*). Numerous simulations have also been performed on the topic (Gamezo *et al.* 2000; Radulescu & Maxwell 2011; Bhattacharjee *et al.* 2013; Han, Wang & Law 2019). Most recently, simulations by Floring, Peswani & Maxwell (2023), modelling the experiment of Bhattacharjee *et al.* (2013), have reported on the initiation mechanism of transverse detonation and that the speed of the transverse detonation is indeed moving at U_{CJ} relative to the upstream gas, a finding that is confirmed in the experiments we report in this work.

In this work we use a narrow detonation channel with mixtures of methane/oxygen/nitrogen. The selected mixtures have relatively high values of reduced effective activation energy and a very abrupt energy release stage in comparison with the induction phase, see table 1 and the associated discussion. As discussed in Shepherd (2009), these

Case	Mixture	P_0 (kPa)	T_0 (K)	P_{vN} [MPa]	T_{vN} (K)	U_{CJ} (m s ⁻¹)	M_{CJ}	$\tau_{I,ZND}$ (μs)	$\tau_{E,ZND}$ (ns)
A/B	CH ₄ -2O ₂ -2N ₂	20.8	299	0.85	1692	2059	5.81	17.8	295
C	CH ₄ -2O ₂ -2.5N ₂	19.3	294.5	0.77	1665	2018	5.74	26.1	379
D	CH ₄ -2O ₂ -2.5N ₂	20.8	294.5	0.83	1667	2020	5.75	24.0	353

Table 1. Calculated detonation parameters. U_{CJ} is the Chapman–Jouguet velocity, M_{CJ} is the Mach number, $\tau_{I,ZND}$ is the induction time and $\tau_{E,ZND}$ is the exothermic time.

properties are associated with highly unstable detonation fronts. One of the unique features of these mixtures is that large regions of partially reacted gas are apparently observed to persist some distance behind the leading front.

Because the studied cases are near the limit of propagation and highly unstable, small changes in the parameters and shot-to-shot differences can dramatically influence the outcome of an individual test. As a consequence, individual tests exhibit a range of reaction outcomes behind transverse waves and the leading shock fronts. Images of the gas-dynamic and chemical-kinetic fields are acquired at MHz rates and with high spatial resolution to allow for the flow dynamics to be quantified. We examine the state of the gas immediately downstream of the low-speed shock to determine conditions that the transverse wave is running through. This approach allows for the quantification and comparison of the speeds of the primary shocks in the transverse detonation wave system. The present study complements and extends our recent examination (Frederick *et al.* 2024) of processes behind leading shock fronts following transverse wave collision. The present work focuses on the reaction processes behind the transverse waves and in particular, the potential for reactant consumption through a transverse wave that has a detonation-like structure.

The experimental apparatus and diagnostics are described in § 2. Results in the form of frames from high-speed movies and associated wave speed analyses are shown in § 3 for four cases of detonations in two mixtures with similar but slightly different compositions. Two classes of transverse waves, reactive and non-reactive, are identified in § 3.2 for each mixture based on the wave speed and schlieren and chemiluminescence images. Examples are shown for each and we provide detailed analysis for one of these mixtures (cases C and D) for which we have highly resolved images from which we can derive wave speed as a function of time as well as evidence from chemiluminescence regarding the extent of reactivity. Combining wave speed data and geometrical configurations of the waves, we have analysed in § 3.3 the influence of wave speed on the reactivity behind the decaying incident and transverse waves. Thermodynamic, one-dimensional reactive flow, and wave speed analyses are employed in § 3.4 to demonstrate the detonative character of the transverse wave observed in case D. This case is further analysed in § 3.5 using the techniques of wave polar analysis to examine in depth the double triple-point configuration that has the features of a Chapman–Jouguet detonation propagating into the shocked-unreacted region behind the leading front.

2. Experiment description

2.1. Detonation channel

Experiments were carried out in the Narrow Channel Facility (NCF), a high-aspect-ratio rectangular channel (8.6:1) developed at the Explosion Dynamics Laboratory at Caltech (Austin 2003) and currently operated at Zucrow Laboratories. Detonations of premixed gases are directly initiated with an acetylene-oxygen driver to create a nominally

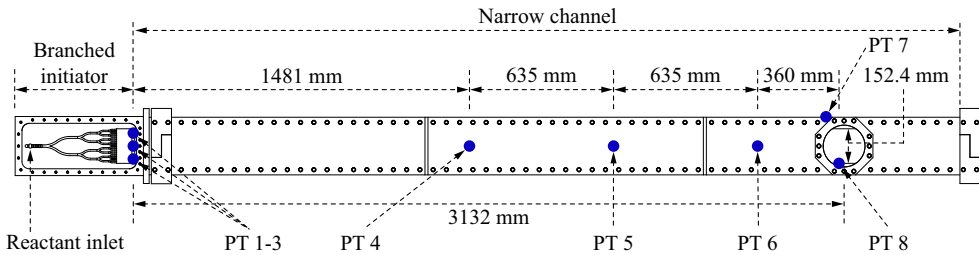


Figure 1. Narrow channel facility schematic and dimensions. High frequency pressure measurement locations labelled as PT 1–8.

two-dimensional detonation wave. Detailed information regarding the design, operation and previous findings with this facility are available in earlier publications (Austin 2003; Austin & Shepherd 2003; Austin, Pintgen & Shepherd 2005; Frederick *et al.* 2019; 2022, 2023, 2024).

2.2. Diagnostics

Two different diagnostic configurations were used in this work. Both utilise the optical access provided by 170 mm fused quartz windows located near the end of the channel, shown in figure 1. The first configuration is an inline lens-type schlieren system, which was used to capture the images shown in figure 4. A pulsed LED is used as the light source. The LED produces an incoherent 635 ± 7 nm light with a 110 ns pulse duration at a 5 MHz pulse frequency. An aspheric condenser lens is placed directly downstream of the light source and passes the focus of the beam through an aperture to enforce a point source. A 250 mm lens is used to collimate the light through the test section and a 500 mm lens is used to collect the light and focus it onto the schlieren cutoff, which is a circular aperture. The light passes through a 631/21 nm single-band bandpass filter to eliminate light emission from the detonation. A total of 128 images are recorded at a rate of 5 MHz on a Shimadzu HPV-X2 high-speed camera with a 150 mm custom camera lens. The Shimadzu HPV-X2 detector has a sensor size of 400×250 pixels. The field of view was 57.32×35.77 mm, yielding a spatial resolution of $143.2 \mu\text{m px}^{-1}$.

The second diagnostic configuration utilised two Shimadzu HPV-X2 cameras to perform simultaneous schlieren and CH^* chemiluminescence imaging at a rate of 1.66 MHz. Images obtained from this set-up are shown in figure 8. For the schlieren configuration f-number f/10 parabolic mirrors are used instead of the lenses used in the inline configuration. The exposure time of the schlieren camera was 200 ns. CH^* chemiluminescence ($\text{A}^2\text{X} \rightarrow \text{X}^2\text{I}_r$) was recorded on a camera placed beneath the schlieren beam path, angled at 9° to have a coincident field of view with the schlieren camera. A 434/17 nm (Semrock 434/17 BrightLine) single-band band-pass filter was used to collect the CH^* signal. The exposure time of the chemiluminescence camera was 300 ns. The field of view obtained by this configuration was larger than configuration one, at 133×83 mm. The resulting spatial resolution was $352.1 \mu\text{m px}^{-1}$. Each camera recorded 128 images per test.

3. Results

Mixtures of stoichiometric methane and oxygen diluted with 40 % and 45 % of nitrogen by volume are examined. This level of dilution is the limit of what is consistently detonable in the NCF at the initial pressure of 20 kPa. Table 1 lists the initial conditions and

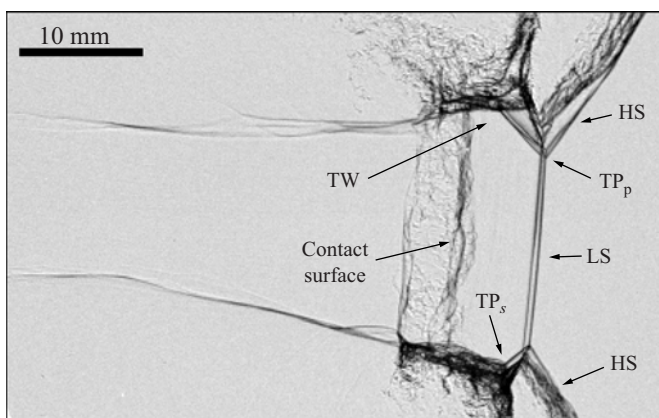


Figure 2. Single schlieren image from case (A) with key features annotated as follows: HS: high-speed shock, LS: low-speed shock, TW: transverse wave, TP_p : primary triple point, TP_s : secondary triple point.

calculated detonation parameters for the four cases studied. All cases were initiated near the same initial pressure and temperature. The uncertainty in initial pressure (P_0) is 2 % and the uncertainty in initial temperature (T_0) and mixture composition is less than 1 %. All parameters are found using the Shock and Detonation Toolbox (EDL 2018) with the GRI3.0 reaction mechanism (Smith *et al.* 1999). Similar values can be obtained by using alternative reaction mechanisms. More importantly, various mechanisms are consistent in predicting the very abrupt energy release region in comparison with the induction region and the large effective reduced activation energy. The ratio of the Zel'dovich-von Neumann-Döring (ZND) induction time ($\tau_{I,ZND}$) to exothermic time ($\tau_{E,ZND}$) is approximately 70. The value of effective reduced activation energy (E_a/RT_{vN}) is approximately 15, where E_a is the activation energy, R is the gas constant, and T_{vN} is the von Neumann temperature. There are only small differences in these characteristics of the two mixtures, and the variations in outcomes we observe between the four cases are due to the intrinsic variability of individual realisations when experimenting with near-limit detonations.

3.1. General description of flow features

The cases in table 1 will each be individually analysed. These cases manifest distinct regimes of transverse wave propagation, but share a common structure that we first discuss. A sample schlieren image from case (A) is labelled with key features in figure 2. Two high-speed shock (HS) waves surround a low-speed shock (LS) wave in the centre of the panel. At the junction of a high-speed shock with the low-speed shock is the primary triple point (TP_p), from which the transverse wave (TW) emanates into the downstream flow field. The TW does not protrude straight back into the flow, as it does with more stable mixtures. Instead, there is an inflection point, labelled as the secondary triple point (TP_s). This structure resembles a double-Mach reflection (DMR) often observed in non-reacting flows. In the terminology used to describe a DMR configuration, the portion of the TW upstream of TP_s is called the primary reflected shock and the portion downstream of TP_s is called the secondary Mach stem. However, in this work since both portions of the wave are moving transverse to the direction of the leading shock, they will collectively be referred to as the TW, unless otherwise noted.

Downstream of the low-speed shock is the contact surface that demarcates the location across which products from the previously reactive leading front and the now non-reactive low-speed shock are separated. The region between the contact surface, low-speed shock

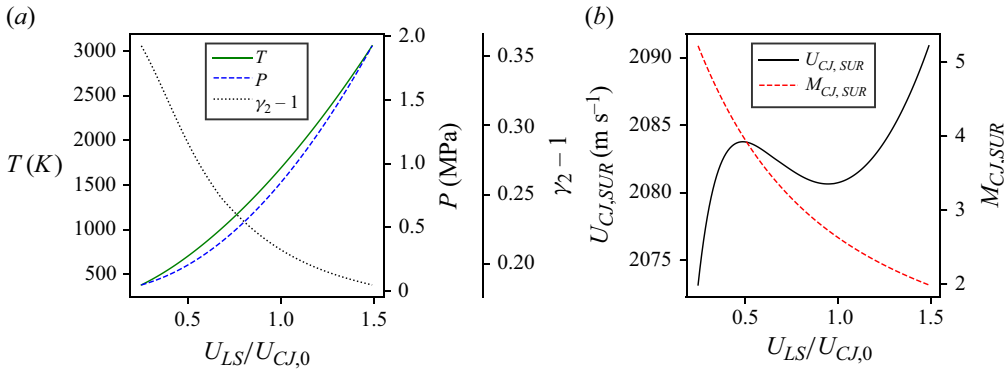


Figure 3. Plot of (a) the pressure, temperature and ratio of specific heats ($\gamma_2 - 1$) and (b) Chapman–Jouguet speed ($U_{CJ,SUR}$) and Mach number ($M_{CJ,SUR}$) within the SUR as a function of the incident shock speed. The mixture composition is that of case (A), where $U_{CJ,0} = 2059 \text{ m s}^{-1}$. Note that $U_{CJ,SUR}$ in (b) is found using a wave speed minimisation algorithm (EDL 2018) with realistic thermochemistry and not by using (3.1).

and the TWs is called the ‘shocked-unreacted region’ (SUR). It contains gases that remain unreacted after being processed by the weak low-speed shock. The designation of ‘unreacted’ is based on multiple factors. These include the lack of any visible chemiluminescence, the lack of intensity perturbation in the schlieren image and chemical reaction simulations that show negligible production of intermediate or reactive species. Due to the low temperature and pressure behind the shock, the computed constant-pressure induction time ($\tau_{I,cp}$) within the SUR is 59 ms, which is three orders of magnitude larger than the ZND induction time (see table 1). Optical measurements of the leading shock speed are used to compute $\tau_{I,cp}$ and are detailed in the next section.

Although the thermodynamic state of the frozen gas within the SUR depends strongly on the low-speed shock speed (see figure 3a), the Chapman–Jouguet speed of a TW propagating into this region does not. Figure 3(b) shows that $U_{CJ,SUR}$ only varies by 17 m s^{-1} with a 2500 m s^{-1} change in the speed of the low-speed shock. This invariance is reconciled by considering that in the strong limit ($M_{CJ} \gg 1$) the approximate expression for Chapman–Jouguet speed is

$$U_{CJ} = \sqrt{2(\gamma_2^2 - 1)q}, \quad (3.1)$$

where q is the difference in stagnation enthalpy between the reactants and products and γ_2 is the ratio of specific heats of the products. Since the composition within the SUR is unchanged by the leading shock, the energy content is the same as the unshocked reactants and U_{CJ} is only weakly affected by the variation in thermodynamic properties across the wave.

3.2. Regimes of transverse wave reactivity

By TW reactivity, we mean the extent and rapidity of reaction downstream of the TW shock front. A select number of images captured for cases (A) and (B) are shown in the left and right columns of figure 4, respectively. Only schlieren imaging was performed for these cases and 5 of the 128 images captured for each case are included. Movies that contain all images are provided in the supplementary material; movie 1 (case (A)) and movie 2 (case (B)). Background subtraction is performed to remove stationary gradients introduced by imperfections in the windows. These images capture a variety of ways in which a TW may appear in highly unstable mixtures.

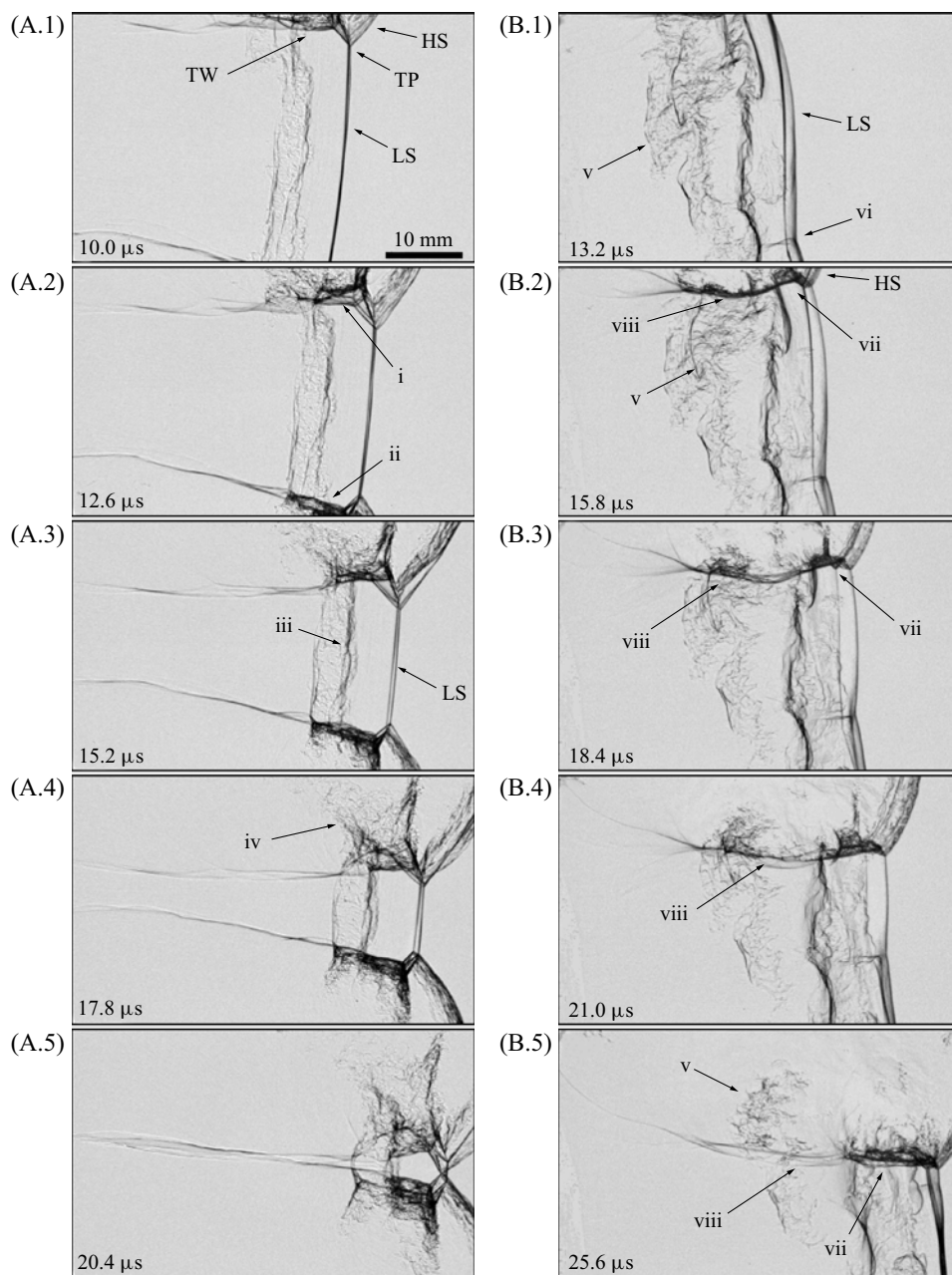


Figure 4. Sequence of select schlieren images showing case (A) in the left column and case (B) in the right column. Key features are called out as: HS: high-speed shock, LS: low-speed shock, TP: triple point, TW: transverse wave. Additional annotations are described in the text.

The reaction progress behind the leading and TWs will be discussed based on the appearance of specific features in the images and detailed chemical-kinetic computations enabled by optical wave speed measurements. For cases (C) and (D), CH^* chemiluminescence allows for direct observation of the combustion processes. However, for cases (A) and (B) careful interpretation of the fluctuations in the schlieren images will be used to interpret reaction progress. The shock normal speed along the leading front is

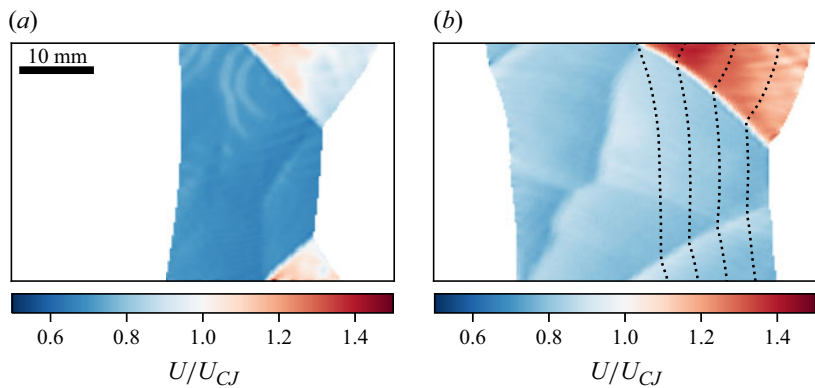


Figure 5. Velocity maps for cases (A) and (B). The dotted lines in panel (b) correspond to the leading edges extracted from panels (B.1)–(B.5) in figure 4.

Case	A		B	C	D
$U_{LS}[\text{m s}^{-1}]$	1416		1678	1558	1534
$U_{LS}/U_{CJ,0}$	0.69		0.81	0.77	0.76
$\tau_{I,LS}[\text{ms}]$	59		1.21	6.89	9.00
Transverse wave	Upper (i)	Lower (ii)	Upstream (vii)	–	Secondary (v)
$U_{TW} [\text{m s}^{-1}]$	1496	1574	1704	796	1978
$U_{TW}/U_{CJ,SUR}$	0.72	0.76	0.82	0.39	0.97
$M_{TW,SUR}$	2.39	2.52	2.46	1.20	3.00
$\tau_{I,TW} [\mu\text{s}]$	8.70	5.00	0.65	1375	0.26
Reactivity	Partial	Partial	Partial	Non-reactive	Detonative

Table 2. Specification of measured average shock speeds and kinetic time scales relevant to TWs in all cases. The speed of the low-speed shock is U_{LS} , the initial mixture CJ speed is $U_{CJ,0}$, the constant-pressure induction time of the low-speed shock is $\tau_{I,LS}$, the speed of the TW is U_{TW} , the SUR CJ speed is $U_{CJ,SUR}$ and the constant-pressure induction time of the TW is $\tau_{I,TW}$. The roman numbers labelling the TWs correspond to those in figure 4 for cases (A) and (B) and figure 16b for case (D).

quantified by extracting the edge location from each schlieren image in time, finding the local spatial gradient of each edge, and computing the normal velocity using a second-order finite-difference method. Further details on the velocity computation can be found in Frederick *et al.* (2023). Figure 5 presents the results of the velocity computation as a velocity-map, where the leading edge velocity found for each panel is plotted in the same spatial coordinate system as the images in figure 4. The dotted lines overlaid in figure 5(b) correspond to the leading edges extracted from panels (B.1)–(B.5) of figure 4. The speed of each shock is normalised by the Chapman–Jouguet speed of the gas it is moving through, with overdriven regions of the front shown in red and under-driven in blue. These maps quantify the velocity oscillation throughout a cell cycle or portion thereof. To find the TW velocity a similar procedure is performed and is described in detail in § 3.4. The measured average wave speeds and induction times for the low-speed and TWs of each case are provided in table 2 and will be referred to throughout this work.

Case (A), shown in the left column of figure 4, depicts the second half of the cycle of cellular detonation propagation. Two families of waves move toward each other and collide (just after panel (A.5)). The collision of the TWs generates a new high-speed shock

(not captured) that marks the beginning of a new cellular cycle. Of particular interest in this case is the reactivity of the two TWs, which are labelled in panel (A.2) of [figure 4](#) as (i) and (ii). These waves move through the unreacted region of gas processed by the low-speed shock, which has an average speed of $0.69 U_{CJ,0}$. As mentioned in § 3.1, the resulting induction time within the SUR is 59 ms. When the gas within the SUR is processed by another shock, in this case the TWs, the resulting degree of reaction depends on the speed of the shock. The upper TW (i) is moving at $0.72 U_{CJ,SUR}$ and appears to partially react the gas within because the wave (i) is dark and wrinkled, indicating reaction. However, there is a region of gas (iv) that makes it downstream of (i) and appears as a distributed perturbation in the density field, which is possibly unreacted or reacting gas. The appearance of (iv) may be reconciled by considering the induction time of (i), which is $8.7 \mu\text{s}$. Taken in context of the images and assuming one-dimensional steady flow, a particle processed by wave (i) in panel (A.1) would not react until it is between panels (A.4) and (A.5). However, over this longer time scale, several outcomes are possible.

One possibility is that unsteady expansion in the flow field behind the leading front causes the reaction to quench. Since the velocity field in region (iv) is unknown and cannot be assumed to be one-dimensional because of the influence of the complex surrounding shock structure, it is not possible to evaluate this possibility based on these measurements. If any reactants do not immediately react upon TW collision, region (iv) will detach from the front completely and become an ‘unreacted gas pocket’ which has been discussed in many studies (Oran *et al.* 1982; Gamezo, Desbordes & Oran 1999; Austin *et al.* 2005; Radulescu *et al.* 2005, 2007; Sanderson *et al.* 2010; Kiyanda & Higgins 2013; Mahmoudi & Mazaheri 2015). Another possibility is that the reactants do rapidly combust, and the released energy does not support the TW because it is released outside of an information path to the TW.

The effect of the extent of reaction immediately behind the TW are modelled in [figure 6](#) by computing the CJ speed of the gas within the SUR when a fraction (X) of the reactants do not combust. For wave (i), only 28.5 % ($X = 0.715$) of the reactants need to burn and support the wave to reach the measured average speed of 1496 m s^{-1} or 0.72 times $U_{CJ,SUR}$, the CJ speed for complete reaction. This calculation supports the idea that a substantial portion of the gas in (iv) is unburned. However, intensity perturbation in a schlieren image does not provide conclusive proof about the reactivity of the gas. A species specific measurement would be required to definitively reach such a conclusion.

The lower TW (ii) has a different character as it moves through the SUR than (i). It is darker and the field of fluctuating intensity behind it occupies a smaller spatial extent than (iv). These observations suggest that the wave is more reactive than (i) and the measured wave speed supports this idea. The average speed of (ii) is $0.76 U_{CJ,SUR}$, with a resulting induction time of $5 \mu\text{s}$. Compared with (i), wave (ii) is only 6 % faster, but has an induction time that is 57 % shorter, as shown in [figure 7](#). At sub- U_{CJ} speeds, even a small increase in wave speed considerably increases the reactivity of the flow behind the wave.

Case (B), shown in the right column of [figure 4](#), shows another example of a reactive TW. Once again, at the beginning of this case (panel B.1) the height of the panel is spanned by a low-speed shock. This shock has an apparent ‘double’ front that is due to three-dimensional effects in the channel (Austin 2003). The furthest upstream portion of this wave is used to compute the average wave speed, which is $0.81 U_{CJ,0}$, and is faster than the low-speed shock in case (A) (see [figure 5](#)). Behind the SUR there is a large region of fluctuating intensity (v), similar in appearance to feature (iv), that exists to a larger extent in the top half of the panel than in the bottom and is likely unreacted gas. In panel (B.2) a high-speed shock (HS) and TW enter the image. The TW can be separated into two parts: a section within the SUR attached to the low-speed shock (vii) and a section (viii)

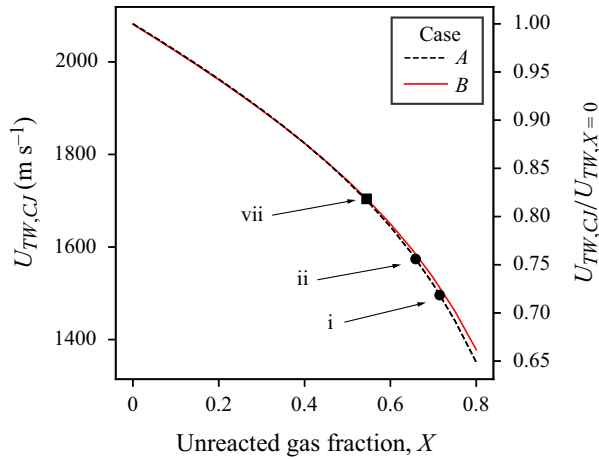


Figure 6. CJ speeds of the TWs in cases (A) and (B) as a function of unreacted gas fraction. The roman numerals correspond to the labelled waves in figure 4. The mixture is defined in terms of X as: $(1 - X)CH_4 + (X)CH_{4,NR} + 2(1 - X)O_2 + 2(X)O_{2,NR} + 2(1 - X)N_2 + 2N_{2,NR}$, where NR identifies a non-reacting molecule.

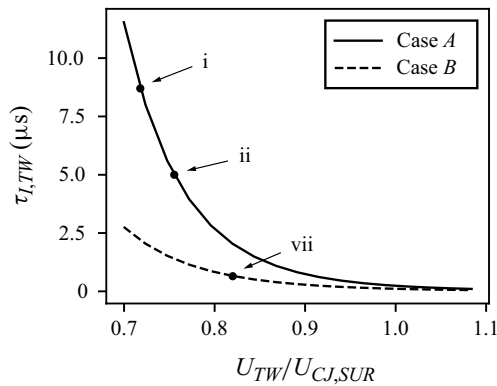


Figure 7. Constant-pressure induction time as a function of wave speed for the gas within the SUR of cases (A) and (B). The roman numerals correspond to the labelled waves in figure 4.

downstream of the contact surface and immediately behind the SUR. Both portions of this wave move at the same speed, which is on average 1704 m s^{-1} or $0.82 U_{CJ,SUR}$.

The Mach number of the wave moving through the SUR (vii) is $M = 2.46$, which is approximately the same strength as those in case (A) (see table 2). However, in contrast to case (A), the TW is much more reactive, with an induction time that is an order of magnitude shorter, $\tau_{I,TW} = 650 \text{ ns}$ (see figure 7). This is because the induction time behind the TW is a function of both the low-speed shock and the TW. The low-speed shock in case (B) is travelling 18 % faster than in case (A) and the resulting induction time within the SUR is nearly fifty times shorter, 1.2 vs 59 ms. Once the TW passes, the combined effect produces a gas with a much shorter reaction time scale. In the schlieren images, this manifests as a compact wave in which the intensity fluctuations downstream of wave (vii) in panel (B.5) quickly becomes homogeneous, with only small pockets of what is likely unreacted gas remaining.

The reactivity of TW section (viii) changes as the case progresses. In panel (B.2) the wave is dark, indicating reaction, and consumes much of the unburned gas pockets (v) ahead of it. By panel (B.5) the TW appears lighter, indicating no reaction, and the gas pockets (v) are still present despite being processed by the TW.

The differences in lead shock behaviour between cases (A) and (B) is understood by examining the velocity maps of each in figure 5. For case (A), the high-speed shocks are overdriven to begin with and then decay to sub-CJ speeds as they approach each other, which is consistent with the typical dynamics of cellular detonation (Shepherd 2009; Frederick *et al.* 2023). However, for case (B), the high-speed shock remains overdriven for the duration of the recording, at an average speed of 2506 m s^{-1} ($1.2 U_{CJ,0}$). This is atypical for cellular detonation, but closely resembles the structure of a spin detonation. Case (D) also presents this wave configuration and a more detailed discussion will be provided in § 3.6.

For the remainder of this paper, the discussion will focus on cases (C) and (D), which show distinct regimes of TW reactivity. These cases were imaged using simultaneous schlieren and CH* chemiluminescence and a select number of panels from each are shown in figure 8. Movies are also provided in the supplementary material; movie 3 (case (C)) and movie 4 (case (D)). The combination of these two diagnostics allows for analysis of the coupled gas-dynamic and chemical-kinetic fields. In figure 8 the schlieren images are displayed on an inverted grey colour scale, such that density gradients appear lighter against the dark background. Due to the large dynamic range of the chemiluminescence intensity, these fields are nonlinearly scaled with a gamma correction ($I_{out} = I_{in}^{\Gamma}$), where $\Gamma = (1/2)$ to portray the full range of the measurement. In case (C), shown in the left column of figure 8, a low-speed shock (i) enters the field of view with a reaction zone (ii) trailing close behind. The low-speed shock is decaying and the reaction zone contact surface decouples from the shock front as time progresses. The average speed of the low-speed shock is $0.77 U_{CJ,0}$, shown in the velocity map of figure 9(a) and histogram in figure 10(a). The resulting induction time within the SUR (iii) is 6.89 ms (see table 2), confirming that the gas within this region is essentially unreacted. At panel (C.3) a triple-point structure (iv) resembling simple Mach reflection enters from the bottom of the panel. The high-speed leading shock (v) associated with this triple point is travelling at an average speed of $0.91 U_{CJ,0}$. The reaction region following the high-speed shock decouples as the wave decays in time. Within the SUR (iii), the TW (vi) is non-reactive based on the lack of trailing chemiluminescence both along the wave and in the region downstream (vii). The non-reactivity of the TW is further verified by considering its average normal speed, which is $0.39 U_{CJ,SUR}$, and the resulting induction time of 1.4 ms. Sanderson *et al.* (2010) modelled similar structures and determined that the kinetics within region (vii) are suppressed by the acceleration and corresponding temperature reduction in the supersonic jet flow. It is the gas within region (vii) that will separate upon TW collision from the main front and form an ‘unreacted gas pocket’.

The TW downstream of the contact surface (viii) does produce a chemiluminescence signal. The cause for this is not immediately clear as the TW does not move through any visible unreacted pockets (such as feature (v) in figure 4(B.2)). It is our hypothesis that the chemiluminescence signal produced behind the TW is caused by the excitation of ground-state CH that exists following the decoupling of the wave that now appears as the low-speed shock. The decoupling event, which took place before image acquisition began, occurs when energy release behind the wave can no longer compete with the retarding effects of the flow expansion. At the moment of decoupling the pressure and temperature drop sharply, freezing any chemical reactions in progress. Following decoupling, only very slow chemical reaction occurs, as evidenced by the gradual chemiluminescence decay in

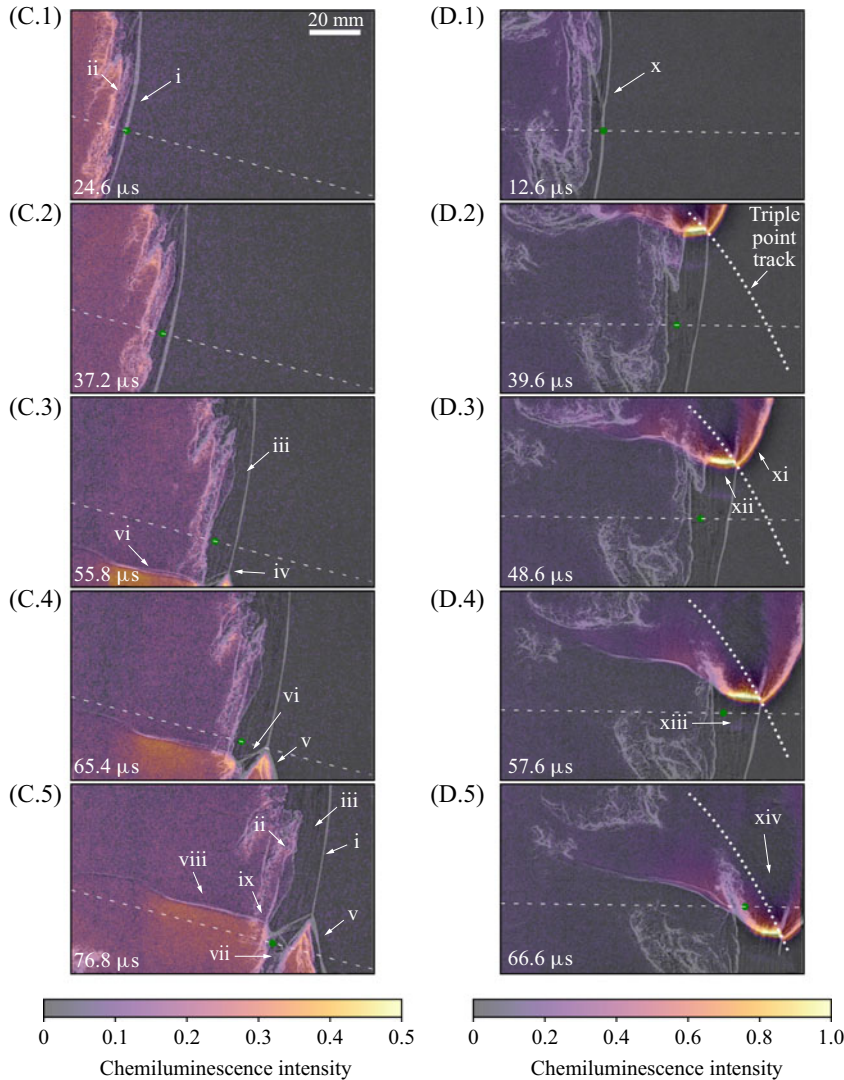


Figure 8. Sequence of overlaid schlieren and chemiluminescence images for case (C) in the left column and for case (D) in the right column. The roman numerals label key features discussed in the text. The dashed line overlaid on each panel corresponds to the selected region in [figure 11](#).

the downstream region of panels (C.1)–(C.3). We speculate that when the TW passes, the frozen intermediate species are brought to a higher temperature and pressure, causing the remaining ground state CH molecules to be excited to a higher electronic level, producing a chemiluminescence signal upon relaxation.

Case (D) (right column of [figure 8](#)), like case (C), begins in panel (D.1) with a low-speed shock (x) that extends the height of the panel and is moving with an average speed of $0.76 U_{CJ,0}$. However, unlike case (C), the Mach-reflection structure that enters the field of view, in panel (D.2), consists of a high-speed shock (xi) and TW (xii) that are both reactive. The high-speed shock is overdriven and reactive for the entirety of the observation period, with average speed of $1.11 U_{CJ,0}$ (see [figure 10b](#)). The reactive TW (xii) wave produces a stronger chemiluminescence signal than the high-speed shock for the duration of the test.

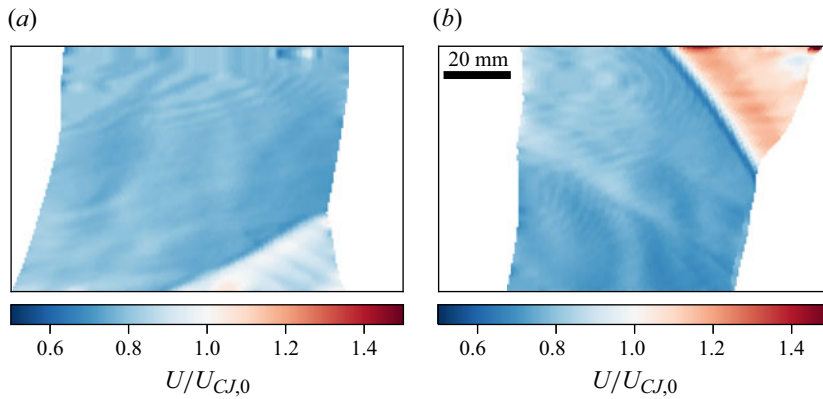


Figure 9. Velocity map for cases (C) and (D) shown in panels (a) and (b), respectively.

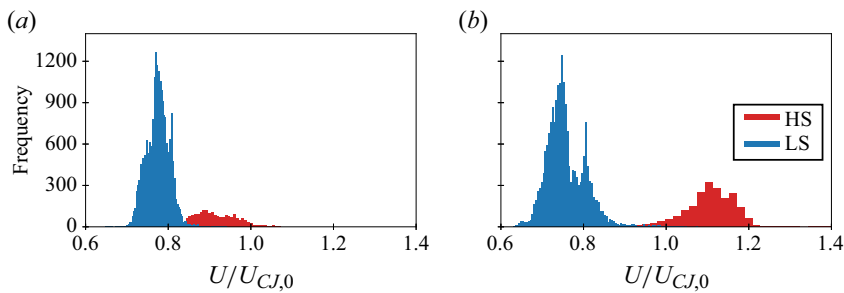


Figure 10. Histogram of leading shock normal velocity for cases (C) and (D) shown in panels (a) and (b), respectively. The measured velocities from the high-speed shock (HS) are shown in red and the low-speed shock (LS) in blue.

We will quantify the speed of this wave in § 3.4 and carefully consider the reactive time scales in § 3.6.1. One point to note is that both the high-speed shock and TW are reactive to such a degree that the emitted chemiluminescence signal appears slightly ahead of the shocks. This is not a physical manifestation, rather the chemiluminescence intensity is so high that it ‘bleeds’ into neighbouring parts of the image due to local pixel saturation.

3.3. Particle path analysis

To investigate the state of the gas that the TWs move through, an analysis of particle paths in the region immediately behind the low-speed shock was performed. Figure 11 shows space-time (x - t) diagrams taken along the dashed lines shown in each panel of figure 8. The diagonal lines represent the spatial trajectory of the chosen particle and are normal to the shock front at the instant the particle crosses the shock. The particle chosen is represented by the green dot in figure 8 and is initially defined in panels (C.1) and (D.1) for case (C) and (D), respectively. In the x - t diagrams the schlieren and chemiluminescence signals are both represented. Above a certain threshold the schlieren signal is binarised and represented in white. The chemiluminescence signal is overlaid in the same colour scale and with the same colour bar as shown in figure 8. In each diagram, the rightmost schlieren trace (white line) corresponds to the leading shock. When the high-speed portion of the leading front crosses the line of extraction ($64 \mu\text{s}$ for case (C) and $59 \mu\text{s}$ for case (D))

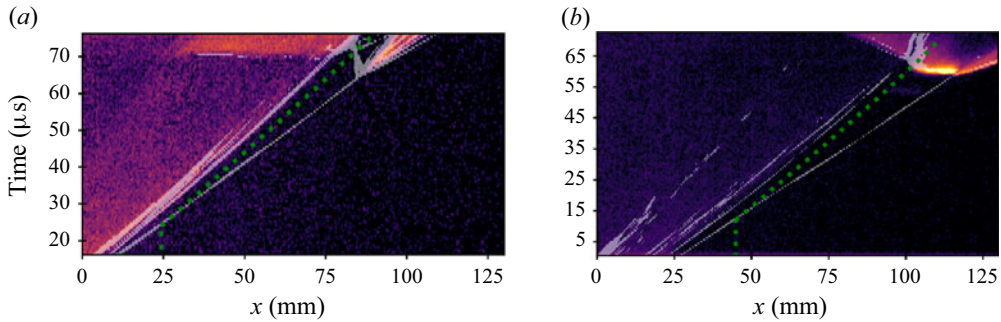


Figure 11. The x - t diagrams showing estimated particle trajectories for cases (C) and (D), respectively. The location of the cuts is shown as a dashed line in figure 8. The green dotted lines are the particle paths corresponding to the particles represented by green dots in figure 8.

the slope of the rightmost schlieren trace steepens to reflect the increased speed of the high-speed shock.

Trajectories for the particles identified by the green dots in figure 8 are proposed as the green dotted lines in figure 11. The lines are estimated using the quasi-unsteady planar reaction zone structure equations of Eckett *et al.* (2000). These equations are derived from the reactive Euler equations and combine the steady ZND reaction zone model with unsteady terms that, after appropriate assumptions are made (see Eckett *et al.* 2000), become a system of ordinary differential equations that requires only the following inputs to solve: initial gas composition, temperature and pressure and the shock speed and acceleration at the instant a particle crosses it. The first three inputs are measured using traditional instrumentation (see § 2.1) and the last two are measured from the leading edge location along the extraction lines in figure 8. This extraction occurs at the times shown in panels (C.1) and (D.1). The values of the shock speed and acceleration for cases (C) and (D) are $U = 0.77U_{CJ,0}$, $0.73U_{CJ,0}$ and $dU/dt = -2400$, -3100 km s^{-2} , respectively. The system of equations is solved using Cantera to incorporate realistic thermochemistry with the detailed chemical reaction mechanism of Smith *et al.* (1999).

For both cases shown in figure 11 the proposed particle paths stay within the SUR region until they reach the TW. The transit time between the low-speed shock and the TW is $\approx 48 \mu\text{s}$ on the postulated paths. However, these paths may be different than we propose. We consider three possible scenarios for the fluid elements or particles moving along these paths.

Scenario 1 is that the particle mixes with products of combustion that are located downstream of the SUR. In panel C.1 of figure 8 the distance to the contact surface, x , is approximately 5 mm. Considering the laminar diffusion problem, where the elapsed time $t = x^2/2D$ and D is the diffusion coefficient of the gas within the SUR ($D \approx 5 \times 10^{-5} \text{ m}^2 \text{ s}^{-1}$), the diffusion time is 250 ms. Even when applying a $20\times$ multiplier to the diffusivity to estimate a turbulent diffusion time, the particle transit time is still three orders of magnitude smaller.

Scenario 2 is that the particle reacts within a propagating adiabatic flame. Singh, Lieberman & Shepherd (2003) calculated that for an initial mixture of stoichiometric methane-air at 300 K, 1 atm, the adiabatic flame speed behind a shock with $M = 4$, which corresponds to the strength of the low-speed shocks considered here, is approximately 250 cm s^{-1} . To cross the same 5 mm distance examined above would require 2 ms (laminar) or $100 \mu\text{s}$ (turbulent), each of which is longer than the particle transit time.

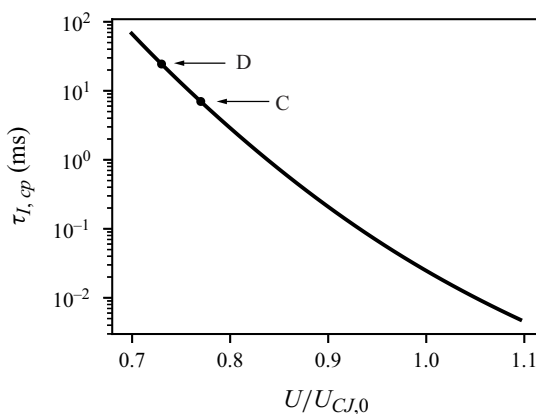


Figure 12. The constant-pressure induction time as a function of normalised wave speed for a mixture of $\text{CH}_4\text{-2O}_2\text{-2.5N}_2$, where $T_0 = 295\text{ K}$ and $P_0 = 20\text{ kPa}$.

Scenario 3 is that the particle undergoes adiabatic explosion within the SUR. The constant-pressure induction time is plotted in figure 12 as a function of normalised shock speed. As the wave speed drops below $U_{CJ,0} = 1$ the increase in induction time is nearly exponential. For cases (C) and (D), the resulting induction time is about 10 ms. Of course, these waves are also decelerating so the flow behind the front is expanding and cooling, which serves to suppress the reaction. The critical expansion time scale that can be supported before reaction is impossible can be estimated with the critical decay rate model (see (57) in the supplement of Frederick *et al.* 2024). For these cases, the critical value is $\approx 35\text{ ms}$ and the time scale defined by the measured shock acceleration is $\approx 200\text{ }\mu\text{s}$, further confirming that adiabatic explosion is extremely unlikely to occur along the particle paths. This means that gas processed by the low-speed shock for these cases accumulates in the SUR and, in the instance of case (D) (panel (b) of figure 11), only reacts when it passes through the reactive TW. For case (C) (panel (a) of figure 11) the gas accumulates in the region downstream of the high-speed shock and TW. This region likely detaches from the main front upon TW collision and forms an unreacted gas pocket, although not directly observed in this instance.

3.4. Shock speed analysis

To further explore the reactivity induced by the TW in case (D), the speed of the wave is computed and compared with $U_{CJ,SUR}$. The first step in performing this analysis is to extract the location of the TW. Figure 13(a) shows a single schlieren image of case (D) with the extracted TW location shown in green, along with the high-speed shock in red, the low-speed shock in blue and the triple point in yellow. The TW is extracted at all panels in time in a method similar to the leading edge. The spatial coordinates of the extracted TW are shown in figure 13(b) and are presented in a reference frame attached to the triple point, where $x = 0$ corresponds to the triple-point location. A map of the vertical (y -direction) component of velocity of TW is shown in figure 13(c). The map was computed using the extracted edges and a second-order finite-difference method. The velocity of the TW remains relatively constant in time and space, slightly accelerating in the top of the panel and with some low-speed fluctuations in the downstream portion due to errors in edge detection.

Time traces of normalised velocity for a point on each shock taken 5 mm from the triple point are shown in figure 14. The speeds are normalised by the calculated U_{CJ}

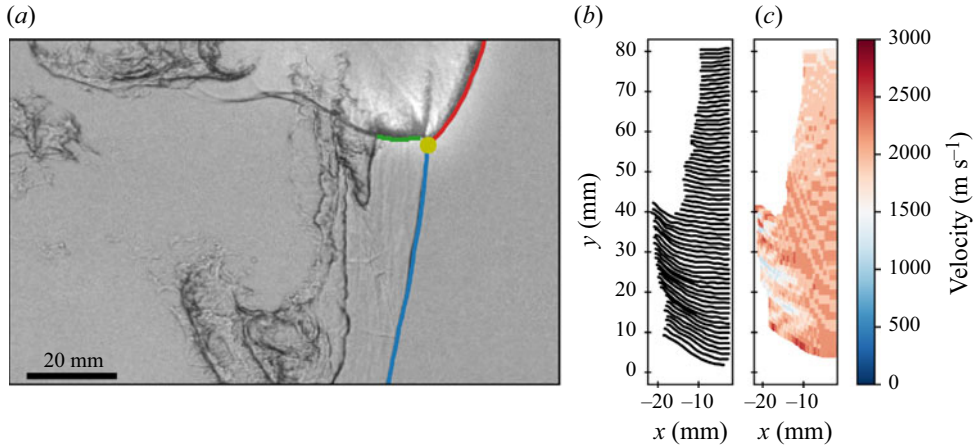


Figure 13. (a) Representative schlieren image of case (D) highlighting the three primary waves: high-speed shock: red, low-speed shock: blue, and transverse detonation: green. (b) The spatial coordinates of the extracted transverse detonation and (c) the velocity map of the transverse detonation in the reference frame of the triple point. The coordinate $x = 0$ corresponds to the triple-point location.

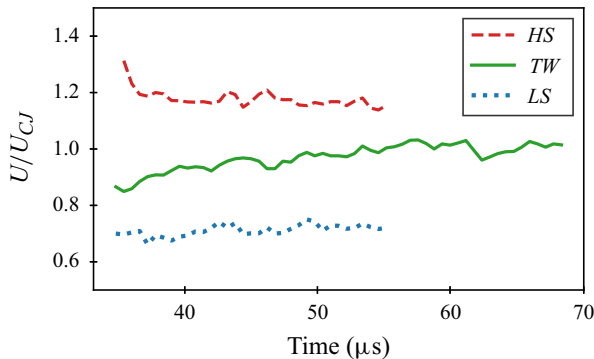


Figure 14. The normalised shock speed of the high-speed shock $U_{HS}/U_{CJ,0}$ (red), transverse detonation $U_{TW}/U_{CJ,SUR}$ (green) and low-speed shock $U_{LS}/U_{CJ,0}$ (blue).

appropriate to mixture ahead of the wave. For the high- and low-speed shocks the initial mixture conditions are used. For the TW it is assumed that the gas state behind the low-speed shock is frozen. The post-shock state is calculated with the measured low-speed shock speed and used to compute U_{CJ} of the shocked-unreacted gas, which is 2039 m s^{-1} . Applying this normalisation, it becomes apparent that the TW moves at or near U_{CJ} for the duration of the test, confirming that this wave is indeed a Chapman-Jouguet detonation. A similar result has recently been obtained in the simulations performed by Floring *et al.* (2023). The low-speed shock is under-driven, moving at an average speed of $0.71 U_{CJ,0}$. The high-speed shock travels at a near constant speed, with an average of $1.18 U_{CJ,0}$.

3.5. Triple-point configuration model

Closer inspection of the triple-point configuration of case (D) reveals that it consists of two triple points, like that of a double-Mach reflection in non-reacting flows (Ben-Dor 2007). These types of reflection geometries, which manifest when a supersonic flow turns at a large angle, have often been modelled in the pressure–flow deflection angle plane

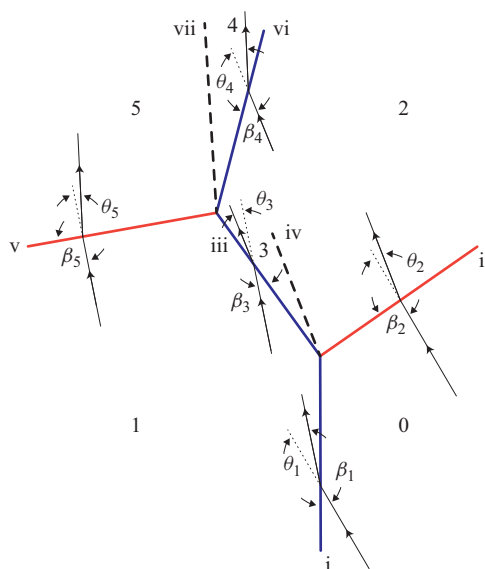


Figure 15. Triple-point configuration and wave angles. Wave assignments for the primary triple point - i: low-speed shock (incident), ii: high-speed shock (Mach stem), iii: TW, iv: shear layer. Wave assignments for the secondary triple point - iii: low-speed shock (incident), v: high-speed shock (Mach stem), vi: TW, vii: shear layer.

(Oppenheim, Smolen & Zajac 1968). This type of analysis enables all flow properties and wave strengths to be estimated in the vicinity of the shock structure. Specific to detonations, implementation of this analysis has proven particularly useful when study of these flows was restricted to single-shot images (Voytsekhovskiy *et al.* 1963; Urtiew 1970; Barthel 1972; Subbotin 1975b) and detailed quantification of wave velocity could not be performed. Pintgen *et al.* (2003) employed a non-reacting version of this analysis to estimate the TW strength for mixtures of various degrees of stability. Sanderson *et al.* (2010) developed a partially reacting version of these relations to propose a mechanism by which unreacted jets are formed in regions bounded by shear layers behind the front. A similar analysis is performed in this work to determine if a model can predict the observed structure containing the transverse detonation and to compare with the experimentally measured wave speeds.

The geometry and states of the wave configuration being solved for is shown schematically in figure 15. Flow states are labelled with numbers (0–5) and the shocks/shear layers with roman numerals (i–vii). Shocks i, ii and iii intersect at the primary triple point and shocks iii, v and vi intersect at the secondary triple point. Shock iii belongs to both triple-point realisations and serves as the TW for the primary and the incident shock for the secondary. In order to account for the strong chemiluminescence that is clearly observed in case D (see figure 8), shocks ii and v are considered reactive (shown in red) and the others (i, iii, vi) are non-reactive or frozen (shown in blue).

This analysis further assumes that the flow is steady in the reference frame of the primary triple point, that the secondary triple point moves at the same velocity and in the same frame of reference as the primary (Sanderson *et al.* 2010), and that the shocks are straight. The shock/detonation polar solution is then calculated by numerical solution using realistic thermochemistry. The equation set and methodology is given in Appendix A,

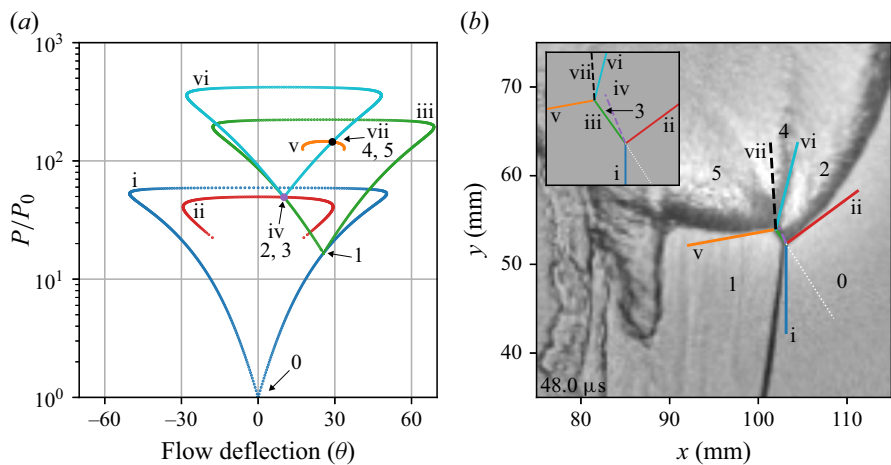


Figure 16. (a) Pressure-deflection diagram illustrating the reactive triple-point solution. (b) The model wave system overlaid on the schlieren image. The flow states are labelled with numbers (0–5) and the shocks/shear layers are labelled with roman numerals (i–vii). The model parameters are: $P_0 = 20.78$ kPa, $T_0 = 294.5$ K, $X_0 = \text{CH}_4\text{-2O}_2\text{-2.5N}_2$, $\beta_1 = 32.5^\circ$, $u_0 = 2446$ m s $^{-1}$.

Shock	M_n	U_n/U_{CJ}	β°	θ°
i	3.74	0.65	32.5	25.5
ii	6.94	1.21	86.1	10.1
iii	1.66	0.49	151.3	–15.4
v	3.45	1.02	86.7	3.5
vi	1.65	0.54	36.6	18.9

Table 3. Shock wave parameters corresponding to the triple-point configuration solution shown in figure 16(a). M_n is the upstream, relative Mach number evaluated normal to the shock and U_n/U_{CJ} is the wave speed normalised to the computed CJ wave speed for the appropriate upstream mixture.

Two parameters must be specified, in addition to the known initial gas state and composition (P_0 , T_0 and X_0 , given in § 2.1), to solve the triple-point configuration. We choose to assign the incoming flow velocity u_0 and the shock angle of the primary incident wave β_1 . Both of these values are measured by extracting the primary triple-point location in time as to record the triple-point track, shown in figure 8(D.2–D.5). The angle formed between the triple-point track and the low-speed shock is β_1 . In the quasi-steady reference frame of this analysis the incoming flow moves parallel to the triple-point track and therefore the average speed of the triple point along its track is u_0 .

A single schlieren image from case D, taken at $t = 48$ μs , is used to extract the parameters β_1 and u_0 and generate a solution to triple-point configuration. Figure 16a shows the locus of shock polars that define the solution. All labelled flow states and features correspond to those in figure 15. Tables 3 and 4 provide the values of oblique shock and thermodynamic parameters, respectively. For a non-reacting solution, the polars representing waves (i) and (ii) and waves (iii) and (v) would each be coincident because each set of waves processes the same upstream flow. However, in this model, where waves (ii) and (v) are reactive, for a given flow deflection angle the pressure rise across the reactive wave is less than that of the non-reactive wave. This is easily reconciled by considering that the pressure at the CJ point is always less than at the von

State	P (kPa)	T (K)	u (m s ⁻¹)	$\tau_{I,ZND}$ (μ s)	$\tau_{E,ZND}$ (ns)	$\tau_{I,cp}$ (μ s)
0	20.78	295	2446	–	–	–
1	344.6	941	2077	–	–	37×10^4
2	1025	3423	683	1.02	139	1.00
3	1025	1206	1872	–	–	1795
4	3015	1519	1577	–	–	24.4
5	3015	3527	1009	0.34	48	0.33

Table 4. Flow state parameters corresponding to the labelled states in figure 16. Here, u is the velocity in the direction θ , $\tau_{I,ZND}$ and $\tau_{E,ZND}$ are the induction and exothermic times, respectively, computed with the modelled shock velocities using the ZND equations and $\tau_{I,cp}$ is the induction time computed with the constant-pressure model.

Neumann point. Additionally, the polars for waves (ii) and (v) do not form closed curves because if the incoming flow angle β is too shallow, the component of the flow moving normal to the shock is less than the CJ speed and a reactive equilibrium solution is not possible.

The computed wave system is overlaid with an enlarged view of the relevant portion of the schlieren panel in figure 16(b). The wave system calculation is highly idealised and does not reflect the curvature of waves away from the critical point. The wave angles shown represent the values close to triple points and the length of the wave (iii) has been scaled to correspond to the image. The inset at the top left corner of figure 16 depicts the wave system with the shock (iii) and shear layer (iv) resolved. The white dotted line to the right of shock (i) indicates the triple-point path, which is used as the incoming flow direction in the analysis. Overall, excellent agreement is shown between the model and the experimental data. Expanding outward from the triple points, the prediction of the shock locations deviates from what is observed, particularly along the reactive waves (ii and v) where wave curvature due to chemical reaction, gradients in the flow, and unsteadiness is evident. Shock (iii), which joins the triple points, is nearly co-linear with the incoming flow, justifying the assumption that the secondary triple point can be treated in the reference frame of the primary.

The wave speeds that are measured in figure 14 are in reasonable agreement with the predictions of the model (see table 3). The difference in normalised speed between the model and experiment vary by 2.5 %, 5 %, 8.5 % for the high-speed shock, transverse detonation and low-speed shock, respectively. These small differences are remarkable considering the assumptions employed in the model. Importantly, both waves (ii) and (v) are predicted to be moving faster than their respective CJ speeds, confirming that they are detonations, while the other three waves are all moving substantially slower than the CJ speed.

3.6. Chemical-kinetic considerations

In order to investigate how the chemical reactions potentially couple with the complex shock structure, numerical simulations are performed in the various flow states of case (D). The simulations are enabled by the solution of the triple-point configuration model and utilise idealised reaction models, either ZND or constant pressure, depending on the situation. These discussions provide further insight into the reaction modes that characterise the transverse detonation wave. In § 3.6.1, we examine the potential for unreacted gas to exist in state 4 and hot reacted gas in state 5. Mixing across the shear layer between these regions is one mechanism of ignition that may lead to the consumption of

any remaining fuel in state 4. In § 3.6.2, we estimate the spatial extent of the reaction zone behind the three reactive waves as determined by energy release profiles. We show that the reaction zone extent for the high-speed shock and transverse detonations are orders of magnitude shorter than that of a CJ detonation. We continue this line of inquiry in § 3.6.3, estimating the potential effect of expansion waves and concluding that due to the vast disparity in scales, the transverse detonation will not be influenced by wave processes in the flow downstream.

3.6.1. Unreacted gases downstream of transverse wave system

Not all gases within the SUR of case (D) (zone 1 in figure 16*b*) are processed by the transverse detonation wave (v) and react rapidly ($\tau_{I,cp} = 330$ ns). Some are processed by wave (iii) and proceed through a series of additional shocks and mix within shear layers; these gases may remain unreacted for an extended period of time. Wave (iii) is angled at 151.3° relative to the incoming flow and therefore the normal velocity component is relatively low, $U/U_{CJ,i} = 0.49$. The resulting induction time within state 3 is long, $\tau_{I,cp} = 1.8$ ms. The gases within state 3 will either mix with those in state 2 or be processed by shock (vi). Upon mixing with state 2, reaction will be rapid because the temperature in state 2 is ≈ 3500 K as the reaction after wave (ii) is quite rapid. Those gases that pass through shock (vi) comprise state 4, which is visible in the schlieren image of figure 16*b*) as the dark region between shock (vi) and shear layer (vii). This feature has been observed experimentally by Subbotin (1975*a*), described in the numerical simulations of Gamezo *et al.* (2000), and named an ‘unreacted tail’. At this point the gas within the tail has been processed by three shocks and the induction time has been shortened to $\tau_{I,cp} = 24.4$ μ s, which may burn out within the observation period. As with shear layer (iv), any gas that mixes across shear layer (vii) between states 4 and 5 will rapidly react due to the high temperature (3527 K) within state 5. Inspection of the schlieren images indicates that the maximum length of the tail is 20 mm and therefore gas within this region likely burns due to mixing or the short induction period.

3.6.2. Scales of chemical reaction

In case (D), for which CH* chemiluminescence measurements were simultaneously obtained, the disparity in chemical scales between the detonative waves can be visualised directly. Figure 17*b*) shows the CH* chemiluminescence image, plotted on a linear colour scale, that corresponds to the schlieren image in figure 16. Using the normal wave speeds obtained with the shock polar model, the thermicity histories behind these waves (normalised by the maximum thermicity of a CJ-detonation in the initial mixture state) are plotted in figure 17*a*). The induction time/length and exothermic time/length are much shorter behind the high-speed shock and transverse detonation than an ideal CJ detonation. The maximum thermicity (analogous to energy release rate) is 2.8 and 8.5 higher for the high-speed shock and transverse detonation, than for the ideal CJ wave. This is evident in the chemiluminescence image where the ratio of average intensity of the transverse detonation is 2.7 times higher than the high-speed shock.

3.6.3. Comparison with expansion scale

Unlike the conventional model of cellular detonation propagation, which is defined by the oscillation of the leading shock front and relatively weak and unsteady TWs, the waves within the transverse detonation system propagate relatively steadily within the period of observation. Considering a detonation to be a competition between chemical kinetics and gas expansion, chemical reactions release energy that advance the wave forward and

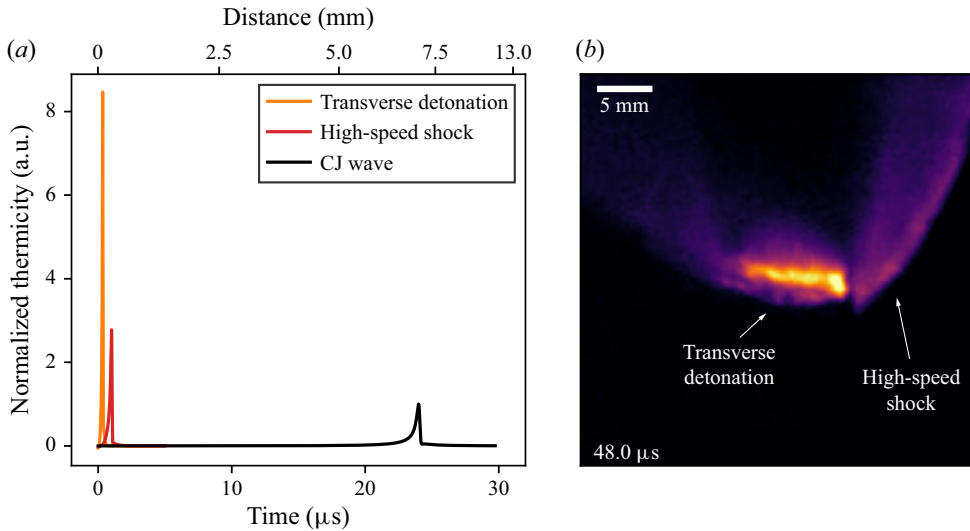


Figure 17. Normalised thermicity magnitude (a) and zoomed in view of the CH* chemiluminescence image (b) for case (D). The field of view and time of the chemiluminescence image in (b) corresponds to the schlieren image in figure 16(b). Unlike the chemiluminescence overlays in figures 8 and 11, the intensity is displayed linearly in (b), $\Gamma = 1$.

expansion processes retard the wave. Within the reaction zone, where unsteady expansion is caused by wave deceleration and curvature, this competition can be modelled as in Eckett *et al.* (2000). However, for case (D) the waves appear steady, and we instead consider the expansion process that occurs behind the reaction zone. Within a channel and when the detonation is unsupported, the expansion process can be modelled as a Taylor wave. The head of the Taylor wave lies at the end of the reaction zone and the tail ends half-way between the head and a bounding surface. For our case (D), we consider the Taylor wave acting in the transverse direction because flow, as designated by shear layer (vii) in figure 15 and 16(b), is primarily vertical. Based on the position of transverse detonation in figures 17(b) and assuming that the bounding surface is the top wall of the channel, the scale of the vertical Taylor wave is ≈ 15 mm. For a wave moving at CJ-speed through the initial mixture, the induction-zone length is 7.23 mm (see figure 17a), which is of the same order as the scale of the Taylor wave. However, for the high-speed shock and transverse detonation, the induction lengths are much smaller, 338 and 137 μm , respectively. Because of this very rapid and short reaction zone length, we conclude that the expansion due to transverse and lateral gradients behind the wave does not compete with the reaction and the wave speeds do not noticeably decay. Although there is no visible evidence of an oscillatory front, it is well established that the characteristic length scales of the front instability are proportional to the ZND reaction zone extent. So it may be possible that the front is unstable with associated TWs that cannot be resolved due to the exceedingly thin reaction zone and resolution limits of the optical system. However, the CJ Mach number of the TW may be sufficiently low that the wave is stable (Austin *et al.* 2005).

4. Conclusion

Highly nitrogen diluted CH₄-2O₂ mixtures were examined using high spatial and temporal resolution imaging. The mixtures studied were all near the limit of continuous propagation

and manifest large instability structures. The observed TWs displayed multiple regimes of reactivity behind the waves and ranged from being non-reactive to highly reactive detonation waves. The locations of the primary shocks were extracted and velocity maps of the leading shock velocity were generated. It was determined that when the flow behind the TW is highly reactive, the leading front tends to be overdriven.

The trajectory of gas particles within the SUR behind the low-speed leading shock was modelled using a quasi-unsteady formulation. The analysis revealed that particles within this region are only processed by the TW. In the case of a non-reactive or partially reactive wave, these particles eventually constitute the gas within unreacted gas pockets that persist behind the front. When the TW is detonative, it rapidly consumes the gas within this region. In highly unstable mixtures with large oscillation in leading shock speed and weak low-speed shocks, TWs appear to play a critical role in ensuring reaction occurs close enough to the front to sustain a propagating detonation.

Measurements of the TWs speeds for all cases allowed for the induction time across these waves to be calculated. These values supported the qualitative observations about the partial reactivity of the TWs for cases (A) and (B). The triple-point configuration structure of the transverse detonation case (case D) was found to very closely match the prediction of a reactive oblique shock model. Using the results of this model, analysis of the kinetic time scales of the gas along various paths through the shock structure revealed that the gases that initially make up the unreacted tails are sufficiently reactive to be consumed before progressing too far behind the front. The gases that proceed through the detonative waves in case (D) have induction times that are sufficiently short that reaction is able to effectively compete with any plausible gas-dynamic expansion process behind, enabling the TWs to propagate steadily at CJ speeds or higher.

Our study was narrowly focused on four tests using two similar but slightly different mixtures. For this reason, we do not make any claims about universality. In the cases we have examined we observe two extreme types of TW behaviour, detonations vs. non-reactive shock waves. We anticipate that similar results could be obtained with marginal detonations in mixtures with similar reduced activation energies (~ 15) and very abrupt energy release regions ($\tau_{I,ZND}/\tau_{E,ZND} \sim 70$) in comparison with the induction-zone extent. Examples include mixtures containing the higher alkanes such as C_3H_8 with similar or higher amounts of nitrogen dilution than used in the present study.

We recognise that a wide range of detonation front characteristics can be observed by varying the mixture composition. For mixtures with much lower reduced activation energy and smoother energy release, e.g. argon diluted H_2-O_2 , we anticipate from past studies (Austin 2003) that the TWs are primarily non-reactive. The experimentation and analysis methods we used could certainly be extended to other mixtures in future studies to explore the range of possibilities between these two extremes.

Supplementary movies. Supplementary movies are available at <https://doi.org/10.1017/jfm.2025.10426>.

Acknowledgements. The authors are grateful to Hadland Imaging for support with the Shimadzu HPV-X2 cameras.

Funding. This work was supported by U.S. Air Force Office of Scientific Research grant FA9550-21-1-0013 (PO: Dr C. Li). M.D.F. acknowledges support from the National Science Foundation Graduate Research Fellowship Program under Grant No. DGE-1333468. One Shimadzu HPV-X2 used in this work was purchased with DURIP grant FA9550-20-1-0226 (PO: Dr C. Li).

Declaration of interests. The authors report no conflict of interest.

Appendix A. Triple-Point Relations

The solution for the double triple-point wave configuration are found by iterative numerical solution of shock-jump conditions matching flow direction and pressure across the contact surfaces emerging from the waves intersection at each triple point. The set of equations is

$$(P_1, T_1, X_0, \theta_1, u_1) = \text{Oshk}_{fr}(P_0, T_0, X_0, \beta_1, u_0), \quad (\text{A1})$$

$$(P_2, T_2, X_2, \theta_2, u_2) = \text{Oshk}_{eq}(P_0, T_0, X_0, \beta_2, u_0), \quad (\text{A2})$$

$$(P_3, T_3, X_0, \theta_3, u_3) = \text{Oshk}_{fr}(P_1, T_1, X_0, \beta_3, u_1), \quad (\text{A3})$$

$$(P_4, T_4, X_0, \theta_4, u_4) = \text{Oshk}_{fr}(P_3, T_3, X_0, \beta_4, u_3), \quad (\text{A4})$$

$$(P_5, T_5, X_5, \theta_5, u_5) = \text{Oshk}_{eq}(P_1, T_1, X_0, \beta_5, u_1), \quad (\text{A5})$$

$$P_3 = P_2, \quad (\text{A6})$$

$$\theta_2 = \theta_1 + \theta_3, \quad (\text{A7})$$

$$P_5 = P_4, \quad (\text{A8})$$

$$\theta_5 = \theta_3 + \theta_4, \quad (\text{A9})$$

where T is temperature, X is gas composition, u is the flow velocity, θ is the flow turning angle and β is the angle of the flow relative to shock. The subscripts identify the flow state shown in figure 15. Equations (A1)–(A5) represent the oblique shock relation (Oshk) that is solved across each wave. The GRI3.0 detailed kinetic mechanism (Smith *et al.* 1999) in Cantera (Goodwin *et al.* 2022) is used for thermodynamic property evaluation. Matching the pressure and flow direction across the shear layers (iv and vi) using (A6)–(A9) completes the system of equations.

Each oblique shock relation Oshk in (A1)–(A5) represents the procedure used to solve the oblique shock-jump conditions. Given the upstream conditions (a) and the wave angle β , the following equations are sequentially solved to obtain the downstream flow thermodynamic state (b), the flow deflection θ and flow speed u_b :

$$(P_b, T_b, \rho_b, X_b) = \text{PostShock}(u_a \sin \beta, P_a, T_a, X_a), \quad (\text{A10})$$

$$u_{b\perp} = \frac{u_a \sin \beta \times \rho_a}{\rho_b}, \quad (\text{A11})$$

$$\theta = \arctan \left(\frac{\left(\frac{\rho_b}{\rho_a} - 1 \right) \tan \beta}{\tan^2 \beta + \frac{\rho_b}{\rho_a}} \right), \quad (\text{A12})$$

$$u_b = \frac{u_{b\perp}}{\sin(\beta - \theta)}, \quad (\text{A13})$$

where ρ is the density, the subscript \perp indicates the value is taken in the direction normal to the shock wave and the subscripts a and b define the upstream and downstream states, respectively. The **PostShock** function in (A10) refers to the solution to the shock-jump conditions, implemented by either the **PostShock_fr** or **PostShock_eq** function in the Shock and Detonation Toolbox (EDL 2018). For (A1), (A3) and (A4), **PostShock_fr** is used to solve the frozen shock-jump equations. For (A2) and (A5), **PostShock_eq** is used to solve for the flow state across the reactive shocks (ii and v), assuming equilibrium composition in the downstream state.

REFERENCES

- ARIENTI, M. & SHEPHERD, J.E. 2005 The role of diffusion at shear layers in irregular detonations. In *The 4th Joint Meeting of the US Sections of the Combustion Institute, Philadelphia, PA*, pp. 1–6.
- AUSTIN, J.M. 2003 The role of instability in gaseous detonation. *PhD thesis*, California Institute of Technology, California, USA.
- AUSTIN, J.M., PINTGEN, F. & SHEPHERD, J.E. 2005 Reaction zones in highly unstable detonations. *Proc. Combust. Inst.* **30** (2), 1849–1857.
- AUSTIN, J.M. & SHEPHERD, J.E. 2003 Detonations in hydrocarbon fuel blends. *Combust. Flame* **132** (1), 73–90.
- BARTHEL, H.O. 1972 Reaction zone-shock front coupling in detonations. *Phys. Fluids* **15** (1), 43–50.
- BEN-DOR, G. 2007 *Shock Wave Reflection Phenomena*. 2nd edn. Springer.
- BHATTACHARJEE, R.R., LAU-CHAPDELAINE, S.S.-M., MAINES, G., MALEY, L. & RADULESCU, M.I. 2013 Detonation re-initiation mechanism following the Mach reflection of a quenched detonation. *Proc. Combust. Inst.* **34** (2), 1893–1901.
- ECKETT, C.A., QUIRK, J.J. & SHEPHERD, J.E. 2000 The role of unsteadiness in direct initiation of gaseous detonations. *J. Fluid Mech.* **421**, 147–183.
- EDL. 2018 SDToolbox: numerical tools for shock and detonation wave modeling. *GALCIT Rep.* FM2018.001. Institute of Technology. Available at <http://shepherd.caltech.edu/EDL/PublicResources/sdt/>.
- EDWARDS, D.H., JONES, A.T. & PHILLIPS, D.E. 1976 The location of the Chapman–Jouguet surface in a multiheaded detonation wave. *J. Phys. D: Appl. Phys.* **9** (9), 1331–1342.
- FLORING, G., PESWANI, M. & MAXWELL, B.M. 2023 On the role of transverse detonation waves in the re-establishment of attenuated detonations in methane–oxygen. *Combust. Flame* **247**, 112497.
- FREDERICK, M.D., GEJJI, R.M., SHEPHERD, J.E. & SLABAUGH, C.D. 2024 Reactive processes following transverse wave interaction. *Proc. Combust. Inst.* **40** (1), 105552.
- FREDERICK, M.D., GEJJI, R.M., SHEPHERD, J.E. & SLABAUGH, C.D. 2022 Time-resolved imaging of the cellular structure of methane and natural gas detonations. *Shock Waves* **32** (4), 337–351.
- FREDERICK, M.D., GEJJI, R.M., SHEPHERD, J.E. & SLABAUGH, C.D. 2019 Preliminary results from narrow channel facility experiments at purdue university. In *AIAA Propulsion and Energy Forum*, pp. 1–8.
- FREDERICK, M.D., GEJJI, R.M., SHEPHERD, J.E. & SLABAUGH, C.D. 2023 Statistical analysis of detonation wave structure. *Proc. Combust. Inst.* **39** (3), 2847–2854.
- GAMEZO, V.N., DESBORDES, D. & ORAN, E.S. 1999 Two-dimensional reactive flow dynamics in cellular detonation waves. *Shock Waves* **9** (1), 11–17.
- GAMEZO, V.N., VASIL'EV, A.A., KHOKHLOV, A.M. & ORAN, E.S. 2000 Fine cellular structures produced by marginal detonations. *Proc. Combust. Inst.* **28** (1), 611–617.
- GOODWIN, D.G., MOFFAT, H.K., SCHOEGL, I., SPETH, R.L. & WEBER, B.W. 2022 Cantera: An object-oriented software toolkit for chemical kinetics, thermodynamics, and transport processes (2.6.0). Available at: doi.org/10.5281/zenodo.6387882.
- HAN, W., WANG, C. & LAW, C.K. 2019 Role of transversal concentration gradient in detonation propagation. *J. Fluid Mech.* **865**, 602–649.
- KIYANDA, C.B. & HIGGINS, A.J. 2013 Photographic investigation into the mechanism of combustion in irregular detonation waves. *Shock Waves* **23** (2), 115–130.
- KOHAMA, S., ITO, T., TSUBOI, N., OZAWA, K. & HAYASHI, A.K. 2024 Two-dimensional detailed numerical simulation of ammonia/hydrogen/air detonation: hydrogen concentration effects and transverse detonation wave structure. *Shock Waves* **34** (2), 139–154.
- LAU-CHAPDELAINE, S.S.-M., XIAO, Q. & RADULESCU, M.I. 2020 Viscous jetting and Mach stem bifurcation in shock reflections: experiments and simulations. *J. Fluid Mech.* **908** (1986), A18.
- MAHMOUDI, Y. & MAZAHERI, K. 2015 High resolution numerical simulation of triple point collision and origin of unburned gas pockets in turbulent detonations. *Acta Astronaut.* **115**, 40–51.
- NG, H.D., RADULESCU, M.I., HIGGINS, A.J., NIKIFORAKIS, N. & LEE, J.H.S. 2005 Numerical investigation of the instability for one-dimensional Chapman–Jouguet detonations with chain-branching kinetics. *Combust. Theor. Model.* **9** (3), 385–401.
- OPPENHEIM, A.K., SMOLEN, J.J. & ZAJAC, L.J. 1968 Vector polar method for the analysis of wave intersections. *Combust. Flame* **12** (1), 63–76.
- ORAN, E.S., YOUNG, T.R., BORIS, J.P., PICONE, J.M. & EDWARDS, D.H. 1982 A study of detonation structure: the formation of unreacted gas pockets. *Symp. (Intl) Combust.* **19** (1), 573–582.
- PINTGEN, F., ECKETT, C.A., AUSTIN, J.M. & SHEPHERD, J.E. 2003 Direct observations of reaction zone structure in propagating detonations. *Combust. Flame* **133** (3), 211–229.
- PINTGEN, F. & SHEPHERD, J.E. 2009 Detonation diffraction in gases. *Combust. Flame* **156** (3), 665–677.

- RADULESCU, M.I. & LEE, J.H.S. 2002 The failure mechanism of gaseous detonations: experiments in porous wall tubes. *Combust. Flame* **131** (1–2), 29–46.
- RADULESCU, M.I. & MAXWELL, B.M. 2011 The mechanism of detonation attenuation by a porous medium and its subsequent re-initiation. *J. Fluid Mech.* **667**, 96–134.
- RADULESCU, M.I., SHARPE, G.J., LEE, J.H.S., KIYANDA, C.B., HIGGINS, A.J. & HANSON, R.K. 2005 The ignition mechanism in irregular structure gaseous detonations. *Proc. Combust. Inst.* **30** (2), 1859–1868.
- RADULESCU, M.I., SHARPE, G.J., LAW, C.K. & LEE, J.H.S. 2007 The hydrodynamic structure of unstable cellular detonations. *J. Fluid Mech.* **580**, 31–81.
- SANDERSON, S.R., AUSTIN, J.M., LIANG, Z., PINTGEN, F., SHEPHERD, J.E. & HORNUNG, H.G. 2010 Reactant jetting in unstable detonation. *Prog. Aerosp. Sci.* **46** (2–3), 116–131.
- SCHOTT, G.L. 1965 Observations of the structure of spinning detonation. *Phys. Fluids* **8** (5), 850–865.
- SHEPHERD, J.E. 2009 Detonation in gases. *Proc. Combust. Inst.* **32** (1), 83–98.
- SINGH, S., LIEBERMAN, D. & SHEPHERD, J.E. 2003 Combustion behind shock waves. In *The Fall 2003 Technical Meeting of the Western States Section of the Combustion Institute*, Paper 03F-29.
- SMITH, G.P., GOLDEN, D.M., FRENKLACH, M., MORIARTY, N.W., EITENEER, B., GOLDENBERG, M., BOWMAN, C.T., HANSON, R.K., SONG, S., GARDINER, JR., W.C., LISSIANSKI, V.V., and QIN, Z. 1999 GRI-Mech. Available at: http://www.me.berkeley.edu/gri_mech/.
- SOW, A., LAU-CHAPDELAINE, S.S.-M. & RADULESCU, M.I. 2021 The effect of the polytropic index γ on the structure of gaseous detonations. *Proc. Combust. Inst.* **38** (3), 3633–3640.
- STREHLOW, R.A. & CROOKER, A.J. 1974 The structure of marginal detonation waves. *Acta Astronaut.* **1** (3–4), 303–315.
- SUBBOTIN, V.A. 1975a Collision of transverse detonation waves in gases. *Fizika Goreniya i Vzryva* **11** (3), 486–491.
- SUBBOTIN, V.A. 1975b Two kinds of transverse wave structures in multifront detonation. *Fizika Goreniya i Vzryva* **11** (1), 96–102.
- TAKESHIMA, N., OZAWA, K., TSUBOI, N., HAYASHI, A.K. & MORII, Y. 2020 Numerical simulations on propane/oxygen detonation in a narrow channel using a detailed chemical mechanism: formation and detailed structure of irregular cells. *Shock Waves* **30** (7–8), 809–824.
- URTIEW, P.A. 1970 Reflections of wave intersections in marginal detonations. *Astronaut. Acta* **15**, 335–343.
- VOYTSEKHOVSKIY, B.V., MITROFANOV, V.V. & TOPCHIYAN, M.Y. 1963 The structure of a detonation front in gases. *Tech. Rep.* Institute of Hydrodynamics, USSR Academy of Sciences.
- XIAO, Q. & RADULESCU, M.I. 2020a Dynamics of hydrogen–oxygen–argon cellular detonations with a constant mean lateral strain rate. *Combust. Flame* **215**, 437–457.
- XIAO, Q. & RADULESCU, M.I. 2020b Role of instability on the limits of laterally strained detonation waves. *Combust. Flame* **220**, 410–428.
- ZHANG, D., DONG, G., CHEN, Y., GUI, M. & WU, Y. 2024 Numerical study on transverse wave structure and blast dynamics of spinning detonation in a square tube. *Phys. Fluids* **36** (5), 056122.